

# Reality of Inverse Cascading in Neutron Star Crusts

Clara Dehman<sup>1,2\*</sup> and Axel Brandenburg<sup>2,3,4,5</sup>

<sup>1</sup> Departament de Física Aplicada, Universitat d'Alacant, Ap. Correus 99, E-03080 Alacant, Spain

<sup>2</sup> Nordita, KTH Royal Institute of Technology and Stockholm University, 10691 Stockholm, Sweden

<sup>3</sup> The Oskar Klein Centre, Department of Astronomy, Stockholm University, AlbaNova, SE-10691 Stockholm, Sweden

<sup>4</sup> McWilliams Center for Cosmology & Department of Physics, Carnegie Mellon University, Pittsburgh, PA 15213, USA

<sup>5</sup> School of Natural Sciences and Medicine, Ilia State University, 3-5 Cholokashvili Avenue, 0194 Tbilisi, Georgia

## ABSTRACT

The braking torque that dictates the timing properties of magnetars is closely tied to the large-scale dipolar magnetic field on their surface. The formation of this field has been a topic of ongoing debate. One proposed mechanism, based on macroscopic principles, involves an inverse cascade within the neutron star's crust. However, this phenomenon has not been observed in realistic simulations. In this study, we provide compelling evidence supporting the feasibility of the inverse cascading process in the presence of an initial helical magnetic field within realistic neutron star crusts and discuss its contribution to the amplification of the large-scale magnetic field. Our findings, derived from a systematic investigation that considers various coordinate systems, peak wavenumber positions, crustal thicknesses, magnetic boundary conditions, and magnetic Lundquist numbers, reveal that the specific geometry of the crustal domain—with its extreme aspect ratio—requires an initial peak wavenumber from small-scale structures for the inverse cascade to occur. However, this extreme aspect ratio limits the inverse cascade to magnetic field structures on scales comparable to the neutron star's crust, making the formation of a large-scale dipolar surface field unlikely. Despite this limitation, the inverse cascade can significantly impact the magnetic field evolution in the interior of the crust, potentially explaining the observed characteristics of highly magnetized objects with weak surface dipolar fields, such as low-field magnetars or central compact objects.

**Key words.** Magnetic fields – stars: neutron – stars: magnetars – stars: interiors – stars: evolution – stars: magnetic field

## 1. Introduction

Magnetars are the most magnetic objects within the population of neutron stars (NSs) (Turolla et al. 2015; Esposito et al. 2021). Their bright X-ray luminosity and occurrence of observed bursts and outbursts are attributed to the restless dynamics and dissipation of a strong magnetic field (about  $10^{14}$  to  $10^{15}$  G) near the NS surface (Thompson & Duncan 1995). Moreover, the large-scale dipolar field on the surface regulates the braking torque responsible for their timing properties (Ostriker & Gunn 1969), resulting in long spin-periods.

The origin and evolution of NS magnetic fields have been long-debated topics. While it is widely accepted that the fossil magnetic field inherited from the progenitor star is insufficient to account for the strongest observed NS fields, additional amplification is necessary. This amplification might occur during the proto-NS stage through a turbulent dynamo process. Additionally, magnetic field amplification can also take place later in an NS's life, either due to the re-emergence of a buried magnetic field driven by Hall drift; see Igoshev et al. (2021) for a review, or through the chiral magnetic instability (CMI) in the NS crust, a microscopic-based mechanism that can explain the formation of large-scale magnetic fields (Dehman & Pons 2024).

Understanding the amplification of the surface dipolar field in magnetars is a challenging task, where macroscopic mechanisms like inverse cascading could be important phenomena to consider. A recent attempt to explain this phenomenon, utilizing an initial turbulent field structure derived from proto-NS dynamo simulations (Reboul-Salze et al. 2021), is presented in

Dehman et al. (2023a). The authors conducted the first 3D coupled magneto-thermal simulation in the crust of a NS, incorporating temperature-dependent microphysical calculations and a realistic stellar structure. The study aimed to determine if starting from such an initial field configuration could explain the observed dipolar field in magnetars. While successful in explaining low-field magnetars, high-field pulsars, and Central Compact Objects (CCOs), this study falls short in explaining the strong surface dipolar field observed in magnetars. The surface dipolar component remained constant over time, with no evidence of an inverse cascade. Other simulations dedicated to the investigation of CCOs have also sought to observe inverse cascading, as seen in Gourgouliatos et al. (2020). However, no inverse cascade was observed in these simulations.

Recent local simulations of the Hall cascade with initial magnetic helicity were presented by Brandenburg (2020). In this study, the author proposed a model suggesting that the large-scale magnetic field of NSs grows as a result of small-scale turbulence. Initially, the magnetic field in young NSs may predominantly exist at small scales, but it could later undergo an inverse cascade, particularly after the crust solidifies. This process implies that the spectral magnetic energy at lower multipoles would increase over time rather than decrease. The study further demonstrates that the resulting dipolar field intensifies approximately linearly with time, typically growing by three orders of magnitude, while thermal dissipation gradually diminishes.

As explained by Brandenburg (2020), the presence of an initial helical magnetic field could be a key factor behind the observed phenomenon of inverse cascading. The simulations further suggest that, even with a relatively weak initial magnetic field, the occurrence of strong inverse cascading is evident.

\* Email: clara.dehman@ua.es

There are two possible sources of magnetic helicity in a NS. One is through dynamo action by neutrino-driven convection in young NS, resulting in oppositely signed magnetic helicities in the two hemispheres (Thompson & Duncan 1995; Brandenburg & Subramanian 2005). Another possible origin of helical magnetic fields in NSs is the CMI. This effect is significant during supernova explosions, throughout the proto-NS phase, and in young NSs. The CMI influences the evolution of the magnetic field in these compact objects, leading to the saturation of magnetic helicity. This, in turn, results in the growth of magnetic fields, which is governed by a conservation law for total chirality (Sigl & Leite 2016; Rogachevskii et al. 2017; Schober et al. 2018; Masada et al. 2018; Brandenburg et al. 2023a,b; Dehman & Pons 2024). Consequently, adopting an initial helical magnetic field provides a realistic foundation for modeling the long-term evolution of NS magnetic fields.

In addition to the significance of the initial helical field in explaining the phenomenon of inverse cascading, several other factors play a crucial role in comprehending the occurrence of inverse cascading within a realistic NS crust. Building upon the findings of Brandenburg (2020), where inverse cascading was first observed in the NS crust, several extensions can be explored. These include incorporating a spherical shell geometry, accounting for the precise aspect ratio determined by applying the Tolman-Oppenheimer-Volkoff equation (Oppenheimer & Volkoff 1939) and employing a realistic nuclear matter equation of state (EoS). Furthermore, instead of imposing periodic boundary conditions, alternative boundary conditions can be considered. Options such as potential boundary conditions at the surface and perfect conductor at the crust-core interface may provide valuable insights. However, at the surface of the star, the most suitable boundary conditions are force-free ones (Akgün et al. 2018; Urbán et al. 2023). Finally, within the NS, the stratification of matter is a crucial consideration. The inclusion of density- and temperature-dependent microphysics becomes imperative for accurately computing the Hall prefactor and magnetic resistivity employed in the evolution equations.

In this article, we aim to explore the potential occurrence of inverse cascading in the crust of a NS by simulating a realistic NS scenario. Our objective is to understand the role of inverse cascading in explaining the strong surface dipole field observed in magnetars. Additionally, we seek to address why this phenomenon has not been identified in previous studies within the NS community. We investigate this process over a time span of  $10^3$  to  $10^5$  years, corresponding to the observed lifetime of magnetars. To achieve these goals, we employ both the PENCIL CODE<sup>1</sup> (Pencil Code Collaboration et al. 2021) and MATINS (Dehman et al. 2023b), taking into account the various relevant parameters.

This paper is organized as follows: In Section 2, we discuss the theoretical formalism of magnetic helicity and its realizability conditions in both Cartesian and spherical coordinates. The numerical setups and the initial conditions are described in Section 3.2. The results of our simulations are presented in Section 4, and we conclude with a discussion of our findings in Section 5.

## 2. Magnetic Helicity and Realizability Condition

### 2.1. General considerations

A helical magnetic field plays an important role in explaining inverse cascading, which might be considered as a candidate to

<sup>1</sup> <https://github.com/pencil-code>

explain the large-scale dipolar field in magnetars. The idea of explaining inverse cascading using a helical field was first proposed by Frisch et al. (1975). The first application to NS physics was explored by Brandenburg (2020). The idea is based on the conservation of magnetic helicity,

$$H_M = \int_V \mathbf{A} \cdot \mathbf{B} dV, \quad (1)$$

where  $\mathbf{A}$  is the magnetic vector potential and  $\mathbf{B} = \nabla \times \mathbf{A}$  is the magnetic field in a volume  $V$ .

Following Brandenburg (2020), simple coordinate-independent measures related to magnetic helicity can be defined in terms of the fractional helicity  $\chi$  and the length scale  $\xi$ , which are introduced through the ratios

$$\langle \mathbf{A} \cdot \mathbf{B} \rangle / \langle \mathbf{B}^2 \rangle \equiv \chi \xi, \quad \langle \mathbf{A} \cdot \mathbf{B} \rangle / \langle \mathbf{J} \cdot \mathbf{B} \rangle \equiv \xi^2. \quad (2)$$

Here, angle brackets denote averages over closed volumes, so  $\langle \mathbf{A} \cdot \mathbf{B} \rangle$  is gauge-invariant. These relations imply that  $\chi^2 = \langle \mathbf{A} \cdot \mathbf{B} \rangle \langle \mathbf{J} \cdot \mathbf{B} \rangle / \langle \mathbf{B}^2 \rangle^2$ , from which the fractional magnetic helicity  $\chi$  is determined.

We recall that for a fully helical Beltrami field with periodic boundary conditions, we have  $\chi = 1$ . When the boundary conditions are non-periodic, for example perfectly conducting on one side and a vertical field condition on the other, Brandenburg (2017) determined analytically the quantity  $\epsilon_m \equiv \langle \mathbf{J} \cdot \mathbf{B} \rangle / (\langle \mathbf{J}^2 \rangle \langle \mathbf{B}^2 \rangle)^{1/2} \approx 0.883$ , which also implies  $\chi = 0.883$ , because in his case  $\langle \mathbf{J} \cdot \mathbf{B} \rangle / \langle \mathbf{A} \cdot \mathbf{B} \rangle = \langle \mathbf{J}^2 \rangle / \langle \mathbf{B}^2 \rangle$ . Thus,  $\chi$  can be close to unity even in the non-periodic case. Furthermore, because  $\chi$  is only an approximate quantity, it can sometimes also exceed unity by a certain amount (Brandenburg 2020). The usage of  $\chi$  approach offers a practical alternative to more rigorous methods that are typically feasible in Cartesian coordinates, which will be discussed next.

### 2.2. Cartesian coordinates

Assuming periodic boundary conditions, the spectra of magnetic energy and magnetic helicity,  $E_M(k)$  and  $H_M(k)$ , can be computed by calculating the three-dimensional Fourier transforms of the magnetic vector potential  $\hat{\mathbf{A}}_k$  and the magnetic field  $\hat{\mathbf{B}}_k$ . The spectra are obtained by integrating  $|\hat{\mathbf{B}}_k|^2$  and the real part of  $\hat{\mathbf{A}}_k \cdot \hat{\mathbf{B}}_k^*$  over shells of constant  $k = |\mathbf{k}|$ , yielding  $E_M(k)$  and  $H_M(k)$ , respectively. Here, the asterisk denotes complex conjugation. These spectra are normalized such that  $\int E_M(k) dk = \langle \mathbf{B}^2 \rangle / 2\mu_0$  and  $\int H_M(k) dk = \langle \mathbf{A} \cdot \mathbf{B} \rangle$  for  $k$  from 0 to  $\infty$ , where  $\mu_0$  is the vacuum permeability. By applying the Schwartz inequality, one can derive the so-called realizability condition (Moffatt 1978),

$$k|H_M(k)|/2\mu_0 \leq E_M(k). \quad (3)$$

The realizability condition serves as an indicator of the degree of helicity within the magnetic field. When Equation (3) is saturated at a particular wavenumber  $k$ , the magnetic helicity is maximal at that wavenumber. If this condition holds true for any arbitrary  $k$ , the system is characterized as being in a state of maximal helicity (Frisch et al. 1975).

For fully helical magnetic fields with (say) positive helicity, i.e.,  $H_M = 2\mu_0 E_M(k)/k$ , Frisch et al. (1975) demonstrated that energy and magnetic helicity cannot cascade directly, i.e., the interaction of modes with wavenumbers  $\mathbf{p}$  and  $\mathbf{q}$  can only produce fields whose wavevector  $\mathbf{k} = \mathbf{p} + \mathbf{q}$  has a length that is equal

or smaller than the maximum of either  $|p|$  or  $|q|$  (Brandenburg & Subramanian 2005), i.e.,

$$|k| \leq \max(|p|, |q|). \quad (4)$$

This implies that magnetic helicity and magnetic energy transform into progressively larger length scales, defining what is known as the inverse cascade. It is expected that the entire spectrum appears to shift to the left, i.e., toward larger length scales, in an approximately self-similar fashion (Brandenburg & Kahnishvili 2017).

### 2.3. Spherical coordinates

In spherical coordinates,  $\mathbf{B}$  can be expressed using two scalar functions  $\Phi(\mathbf{x})$  and  $\Psi(\mathbf{x})$ , following the Chandrasekhar-Kendall formulation (Chandrasekhar 1981):

$$\begin{aligned} \mathbf{B}_{\text{pol}} &= \nabla \times (\nabla \times \Phi \mathbf{r}), \\ \mathbf{B}_{\text{tor}} &= \nabla \times \Psi \mathbf{r}. \end{aligned} \quad (5)$$

Using the notation of Krause & Rädler (1980) and Geppert & Wiebicke (1991), the basic idea is to expand the poloidal  $\Phi$  and toroidal  $\Psi$  scalar functions in a series of spherical harmonics:

$$\begin{aligned} \Phi(t, r, \theta, \phi) &= \frac{1}{r} \sum_{\ell, m} \Phi_{\ell m}(r, t) Y_{\ell m}(\theta, \phi), \\ \Psi(t, r, \theta, \phi) &= \frac{1}{r} \sum_{\ell, m} \Psi_{\ell m}(r, t) Y_{\ell m}(\theta, \phi), \end{aligned} \quad (6)$$

where  $\ell = 1$  to  $\infty$  is the degree and  $m = -\ell, \dots, \ell$  the order of the multipole. Note that in 3D, the toroidal field is a mix of the two tangential components of the magnetic field, whereas the poloidal field is a mix of all three components. This is less trivial than in 2D, where the toroidal part consists of the azimuthal component and the poloidal part consists of the two other components of the magnetic field.

The spectra of the magnetic helicity and the magnetic energy in 3D spherical coordinates are, respectively, defined as follows:

$$H_M(\ell, m; t) = 2 \int \frac{\ell(\ell+1)}{r^2} \Phi_{\ell m} \Psi_{\ell m} r^2 dr, \quad (7)$$

$$E_M(\ell, m; t) = \frac{1}{2} \int \frac{\ell(\ell+1)}{r^2} \left[ \frac{\ell(\ell+1)}{r^2} \Phi_{\ell m}^2 + \Phi_{\ell m}'^2 + \Psi_{\ell m}^2 \right]. \quad (8)$$

Here,  $\Phi_{\ell m}' = \partial \Phi_{\ell m} / \partial r$ . From these expressions, one can define the spectral realizability condition in terms of the poloidal and toroidal scalar functions as

$$2k \Phi_{\ell m} \Psi_{\ell m} \leq \frac{\ell(\ell+1)}{r^2} \Phi_{\ell m}^2 + \Phi_{\ell m}'^2 + \Psi_{\ell m}^2. \quad (9)$$

The pseudo wavenumber  $k = \sqrt{\ell(\ell+1)}/R$  possesses the dimension of inverse length, where  $R$  denotes the surface of our computational domain.

## 3. Numerical Models

### 3.1. Evolution Equations

Using SI units, the equations governing the Hall cascade in NS crust can be written as (Goldreich & Reisenegger 1992)

$$\frac{\partial \mathbf{B}}{\partial t} = \nabla \times \left( -\frac{\mathbf{J} \times \mathbf{B}}{en_e} - \eta \mu_0 \mathbf{J} \right), \quad \mathbf{J} = \frac{1}{\mu_0} \nabla \times \mathbf{B}, \quad (10)$$

where  $e$  is the unit charge,  $n_e$  is the electron density,  $\mu_0$  is the vacuum permeability, and  $\eta$  is the magnetic diffusivity (inversely proportional to the electrical conductivity  $\sigma_e$ ).

A suitable non-dimensional measure quantifying the importance of magnetic diffusivity is the Lundquist number, given by

$$\text{Lu} = B_{\text{rms}} / en_e \mu_0 \eta. \quad (11)$$

Owing to the decay of  $B_{\text{rms}}$ , the value of Lu is time-dependent, but it could in principle also be defined in a position-dependent fashion.

### 3.2. Numerical codes

As mentioned above, we use two numerical codes: the PENCIL CODE<sup>2</sup> (Pencil Code Collaboration et al. 2021) and MATINS (Dehman et al. 2023b). The PENCIL CODE is primarily designed to solve the fully nonlinear, compressible hydromagnetic equations. Its highly modular structure allows for easy adaptation to a wide range of physical setups. It is a high-order finite-difference code, which is efficiently parallelized, enabling therefore high resolution and Lundquist numbers on the order of  $10^3$ . The code can operate on a Cartesian or spherical grid and can be configured to work within a limited sector,  $\theta_1 \leq \theta \leq \theta_2$  and  $\phi_1 \leq \phi \leq \phi_2$ , of a 3D spherical shell. This capability allows us to exclude the axis to avoid singularities and to adjust the aspect ratio as needed. Therefore, the PENCIL CODE is a valuable tool for this study.

On the other hand, MATINS is a 3D code for the MAGneto-Thermal evolution in Isolated NS crusts, based on finite-volume numerical schemes discretized over a non-orthogonal cubed-sphere grid, which effectively resolves the axis singularity problem in 3D spherical coordinates. The cubed-sphere formalism, introduced by Ronchi et al. (1996) and implemented in MATINS by Dehman et al. (2023b), uses one coordinate as the radial direction, similar to spherical coordinates, with the volume composed of multiple radial layers. Each layer is divided into six patches resembling arcs of great circles, forming a spherical shape by inflating the faces of a cube. Each patch is bordered by four others and is described by angular-like coordinates,  $\xi_{cs}$  and  $\eta_{cs}$ , ranging from  $[-\pi/4 : \pi/4]$ . These patches are orthogonal to the radial direction but non-orthogonal to each other, except at the patch centers. This non-orthogonality requires careful distinction between covariant (lower indices) and contravariant (upper indices) field components.

Additionally, MATINS incorporates a spherical star based on a realistic EoS, including corresponding relativistic factors in the evolution equations. It also integrates the latest temperature-dependent microphysical calculations<sup>3</sup>, enabling coupled magneto-thermal simulations if needed (Dehman et al. 2023b,a; Ascenzi et al. 2024).

### 3.3. Initial Conditions

In the following, our objective is to construct an initial helical magnetic field. We use a random initial field with a specific magnetic energy spectrum. It peaks at a certain wavenumber  $k_0$ . For wavenumbers  $k > k_0$ , the spectrum exhibits a distinct inertial range, which may follow a  $k^{-5/3}$  scaling for Kolmogorov-like

<sup>2</sup> <https://github.com/pencil-code>

<sup>3</sup> The public routines implemented in MATINS are available at <http://www.ioffe.ru/astro/conduct/>. For details, see Potekhin et al. (2015).

	$E_A(\mathbf{k})$	$E_M(\mathbf{k})$
1D	$\propto k^0$	$\propto k^2$
2D	$\propto k^1$	$\propto k^3$
3D	$\propto k^2$	$\propto k^4$

**Table 1.** Spectrum of the magnetic vector potential  $\mathbf{A}$  and the magnetic field  $\mathbf{B}$  for  $k \ll k_0$ , depicting the ascending spectra. For more details, see Brandenburg & Boldyrev (2020).

turbulence or a  $k^{-2}$  scaling for wave turbulence (Brandenburg et al. 2015). For  $k < k_0$ , referred to as the sub-inertial range, we adopt a spectrum corresponding to a random vector potential. This implies that in 3D space, the vector potential follows a  $k^2$  spectrum and the magnetic field a  $k^4$  spectrum, as depicted in Table 1. Such a spectrum is often used in the cosmological context, where it is usually referred to as a causal spectrum (Durrer & Caprini 2003). It means that no point is correlated with any other, but the field is additionally divergence-free.

### 3.3.1. The Pencil Code

In Cartesian coordinates, we use a Fourier transform to construct a helical initial condition for the magnetic vector potential  $\mathbf{A}(\mathbf{k})$  by applying the helicity operator  $R_{ij}(\mathbf{k}) = \delta_{ij} - i\sigma\epsilon_{ijl}\hat{k}_l$  with unit vector  $\hat{\mathbf{k}} = \mathbf{k}/|\mathbf{k}|$  on a non-helical transverse field given by:

$$\mathbf{A} = A_0 \frac{\mathbf{k} \times \mathbf{e}}{|\mathbf{k} \times \mathbf{e}|} S_A(k) e^{i\varphi}. \quad (12)$$

Here,  $A_0$  is an amplitude factor,  $\varphi$  with  $|\varphi| < \pi$  are uniformly distributed random phases, and

$$S_A(k) = \frac{k_0^{-3/2} (k/k_0)^{\alpha/2-2}}{[1 + (k/k_0)^{2(\alpha+7/3)}]^{1/4}}. \quad (13)$$

is a function that gives  $E_M(\mathbf{k}) \propto k^\alpha$  for  $k \ll k_0$  and  $E_M(\mathbf{k}) \propto k^{-7/3}$  for  $k \gg k_0$ . For more details on how  $\alpha$  scales with the dimension of the domain, we refer to Table 1 and to the work of Brandenburg & Boldyrev (2020). Here,  $k_0$  is the peak wavenumber of the spectrum. For a given value of  $B_0$ , the resulting initial value of the rms magnetic field,  $B_{\text{rms}}$ , which will be denoted as  $B_{\text{rms}}^{(0)}$ , is usually somewhat larger. For  $k_0/k_1 = 180$ , for example, we find  $B_{\text{rms}}^{(0)}/B_0 \approx 3.2$  when  $\sigma = 0$ , and  $B_{\text{rms}}^{(0)}/B_0 \approx 4.5$  when  $\sigma = 1$ .

Owing to the use of Fourier transforms, our initial conditions are implicitly assumed to be triply periodic in  $\mathbf{x}$ , where  $\mathbf{x} = (x, y, z)$  with  $x_1 < x < x_2$ ,  $y_1 < y < y_2$ , and  $z_1 < z < z_2$ . Boundary conditions (see Section 3.4) will be enforced during the simulations, potentially leading to sharp gradients at the boundaries during the initial time steps. However, this is not a problem later in time.

When using the PENCIL CODE, we can still use the Cartesian initial condition in spherical geometry by replacing  $(x, y, z) \rightarrow (r, \theta, \phi)$ . In that case, the vector potential will no longer be perfectly divergence-free. Also, in the simulations, we are not working in the Coulomb gauge; instead, we are working in the Weyl gauge where the electrostatic potential vanishes. Additionally, the fractional magnetic helicity will be different in this scenario (see Section 2 for coordinate-independent measures of the fractional magnetic helicity).

In the following, we characterize the surface magnetic field in the Cartesian simulations through its two-dimensional energy spectrum,  $E_M(k; x, t)$ , where  $k = |\mathbf{k}|$  and  $\mathbf{k} = (k_y, k_z)$  is the wavevector in the  $yz$  plane. We choose a value of  $x$  that is close

to the outer boundary,  $x_2$ . Owing to the reduction in dimensionality, the otherwise  $k^4$  spectrum of the magnetic field turns into a  $k^3$  spectrum (see Table 1).

### 3.3.2. The MATINS code

According to the Chandrasekhar-Kendall formalism (Chandrasekhar 1981), the magnetic field  $\mathbf{B}$  can be decomposed in spherical coordinates, into poloidal  $\Phi(\mathbf{x})$  and toroidal  $\Psi(\mathbf{x})$  scalar functions, as explained in Section 2.3. The initial magnetic field structure can be constructed by selecting a set of spherical harmonics (see Equation (6)), which defines the angular part of the magnetic field configuration. For additional details, consult Appendix B of Dehman et al. (2023b).

As mentioned at the beginning of Section 3.3, our goal is to start the simulations with a locally isotropic spectrum characterized by an  $\ell^3$  slope<sup>4</sup>. Thus, we express the poloidal scalar function  $\Phi(\mathbf{x})$  as:

$$\Phi(\mathbf{x}) = \frac{1}{r} \sum_{\ell m} \phi_{\ell m}(r_a) f_\ell(r) Y_{\ell m}(\theta, \phi), \quad (14)$$

with

$$\Phi_{\ell m}(r_a) = \sum_{\ell m} \frac{1}{\ell(\ell+1)} \int dS_r B^r(r_a, \theta, \phi) Y_{\ell m}(\theta, \phi). \quad (15)$$

Here,  $\Phi_{\ell m}(r_a)$  represents the weights of the multipoles, extracted from simulations using the PENCIL CODE at a given radial layer  $r_a$  near the surface of the star  $R$ ,  $dS_r$  is the surface differential,  $f_\ell(r)$  is the radial spectral mode function, and  $B^r$  is the contravariant radial component of the magnetic field, as MATINS employs a non-orthogonal cubed-sphere metric. This selection ensures the achievement of the desired locally isotropic  $\ell^3$  initial sub-inertial range.

To establish a locally isotropic magnetic field across all radial layers, we define  $f_\ell(r)$  as follows:

$$f_\ell(r) = \sin(k_\ell^{\text{eff}} r), \quad k_\ell^{\text{eff}} = \iota \sqrt{\ell(\ell+1)}/R, \quad (16)$$

where  $k_\ell^{\text{eff}}$  is the radial wavenumber. The choice of  $k_\ell^{\text{eff}}$  is motivated by the dimensional argument of the realizability condition; see Equations (3) and (9). The parameter  $\iota$  is a constant that can be adjusted in our simulations to ensure the desired number of multipoles along the radial direction, as one can define  $k_0 R \propto \iota \ell_0$ . Here,  $k_0$  and  $\ell_0$  are the peak wavenumber and degree of the multipoles in the spectrum, respectively. For  $\iota = 1$ ,  $k_\ell^{\text{eff}}$  simplifies to the wavenumber  $k$ .

The choice of the radial function  $f_\ell(r)$ , as defined, does not adhere to the potential and perfect conductor boundary conditions imposed at the surface and the crust-core boundary, respectively. However, considering our goal of conducting simulations with a large Lundquist number on the order of 100...1000, it is anticipated that the initial condition's influence on the global evolution will be minimal. Also, as discussed above, the magnetic field is expected to readjust to the imposed boundary conditions after a few evolution time steps, a behavior also observed in the PENCIL CODE simulations. It is worth noting that, in order to construct an initial field that respects boundary conditions, the solution of Bessel functions would be necessary, which inspired our current choice of the sine function.

<sup>4</sup> The plotted energy spectrum (Equation (8)) in MATINS is a 2D spectrum decomposed into spherical harmonics along  $\theta$  and  $\phi$  coordinates

To construct an initial helical field, the toroidal scalar function  $\Psi(\mathbf{x})$  must be expressed as

$$\Psi(\mathbf{x}) = k \Phi(\mathbf{x}), \quad (17)$$

where  $k = \sqrt{\ell(\ell+1)}/R$ . Upon examining Equation (9), it becomes apparent that, at the surface of the star, the ratio of the left-hand side to the right-hand side approaches one, indicating that the magnetic field tends toward maximal helicity. However, the presence of the  $\Phi_{\ell m}^{\prime 2}$  term on the right-hand side of Equation (9) prevents the Chandrasekhar-Kendall formalism from achieving a fully helical field. It is worth noting that different choices of the radial function also ensure a helical field if Equation (17) is enforced.

The magnetic field components are computed using the curl operator applied to  $\Phi(\mathbf{x})$  and  $\Psi(\mathbf{x})$  in cubed-sphere coordinates; see Dehman et al. (2023b). This method guarantees that the initial magnetic field structure is divergence-free up to machine precision and effectively avoids the axis-singularity problem inherent in spherical coordinate. Our experience shows that this approach yields satisfactory results for our objectives, particularly in generating a visually more locally isotropic field, as will be demonstrated in Section 4.

### 3.4. Boundary Conditions

In our simulations, we confine the magnetic field to the crust of the star. Consequently, the inner boundary conditions are imposed by requiring the normal (radial) component of the magnetic field to vanish at the lower boundary ( $r = r_0$ ). This physically represents the transition from normal to superconducting matter. Under these assumptions, the Poynting flux at the inner boundary is zero, preventing any energy flow into or from the core of the star. In the PENCIL CODE, this boundary condition, in terms of the magnetic vector potential, translates to

$$\frac{\partial A_r}{\partial r} = A_\theta = A_\phi = 0 \quad (r = r_0). \quad (18)$$

On the other hand, MATINS imposes inner boundary conditions on both the electric and magnetic fields. This stems from the direct evolution of the magnetic field components within the code. In cubed-sphere coordinates, the tangential components of the electric and magnetic fields at the inner boundary are expressed as follows:

$$\begin{aligned} E^{\xi,\eta}(r_0) &= \frac{1}{2} E^{\xi,\eta}(r_0 + dr), \\ B^{\xi,\eta}(r_0 - dr) &= \frac{r_0}{r_0 - dr} B^{\xi,\eta}(r_0). \end{aligned} \quad (19)$$

In the equations above, we have omitted the angular coordinates for brevity. The radial coupling among the nearest neighbors, occurring over a distance  $dr$ , is implemented to address the issue of odd-even decoupling or checkerboard oscillations, which arise from two slightly different solutions—one corresponding to odd grid points and the other to even grid points. This phenomenon is a known issue with second-order central difference schemes when applied to the second derivative of a function. By adopting this approach, we mitigate tangential currents at the crust-core interface and improve stability during the evolution.

At the outer boundary, all components of the magnetic field are continuous, if surface current sheets are excluded. In the PENCIL CODE simulations, the magnetic field is radial at the outer

boundary, which, in terms of the magnetic vector potential, translate to

$$A_r = 0, \quad \frac{\partial A_\theta}{\partial r} = -\frac{A_\theta}{r}, \quad \frac{\partial A_\phi}{\partial r} = -\frac{A_\phi}{r} \quad (r = R). \quad (20)$$

Along the  $\theta$  (or  $y$ ) direction, perfect boundary conditions were imposed. Moreover, in the PENCIL CODE, we sometimes use periodic boundary conditions.

Conversely, in MATINS, we implement an external potential (current-free) solution for the magnetic field at the surface of the star, governed by  $\nabla \times \mathbf{B} = 0$  and  $\nabla \cdot \mathbf{B} = 0$ . This magnetic field is expressed as the gradient of a magneto-static potential that satisfies the Laplace equation (Dehman et al. 2023b). The potential is expanded in spherical harmonics, allowing us to express the three components of the magnetic field at the surface of the star as

$$B^r = B_0 \sum_{\ell m} (\ell + 1) b_\ell^m Y_{\ell m}, \quad (21)$$

where  $B_0$  is a normalization factor and  $b_\ell^m$  corresponds to the dimensionless weight of the multipoles:

$$b_\ell^m = \frac{1}{B_0(\ell + 1)} \int \frac{dS^r}{r^2} B^r Y_{\ell m}. \quad (22)$$

The angular components of the magnetic field are given by:

$$B^\theta = -B_0 \sum_{\ell m} b_\ell^m \frac{\partial Y_{\ell m}}{\partial \theta}, \quad (23)$$

$$B^\phi = -\frac{B_0}{\sin \theta} \sum_{\ell m} b_\ell^m \frac{\partial Y_{\ell m}}{\partial \phi}, \quad (24)$$

which are then converted into the  $B^\xi$  and  $B^\eta$  components on the cubed-sphere grid within the code. For a detailed description of the magnetic boundary condition in MATINS, see Dehman et al. (2023b).

### 3.5. Units and simulation parameters

For the PENCIL CODE simulations, we present the results in nondimensional form by introducing the following units:

$$[x] = R, \quad [t] = R^2/\eta, \quad [\mathbf{B}] = en_e\mu_0\eta. \quad (25)$$

This implies that the current density is measured in units of  $[\mathbf{J}] = [\mathbf{B}]/\mu_0 R$ . To express the PENCIL CODE results in dimensional units, we multiply by the appropriate units described above. Moreover, we consider a Hall cascade with a characteristic wavenumber  $k_0$ , which represents the initial peak of the spectrum. This peak wavenumber is related to the spherical harmonic degree  $\ell_0$ , where most of the energy is concentrated, through the relation  $k_0 = \sqrt{\ell_0(\ell_0 + 1)}/R$ . We set  $1/en_e\mu_0 = 1$  and adopt a time-dependent prescription for the magnetic diffusivity  $\eta$ :

$$\eta(t) = \begin{cases} \eta_0 & \text{if } t \leq 0.1 \\ \eta_0 e^{-0.4t} & \text{if } t > 0.1 \end{cases} \quad (26)$$

Here,  $\eta$  remains constant throughout most of the evolution time, except for the very late stage (after  $t > 0.1$ ). This adjustment ensures an increase in the Lundquist number at later times ( $t > 0.1$ ) if the simulation continues for that duration. Additionally, for the PENCIL CODE, we use different mesh points depending on

the aspect ratio considered in each simulation. The specific mesh points used are detailed in Table 2.

In MATINS, we use physical units commonly applied in astrophysics, defined as follows:

$$\begin{aligned} [x] &= 1 \text{ km}, & [t] &= 1 \text{ yr}, & [\mathbf{B}] &= 1 \text{ G}, \\ [J] &= 1 \text{ G km}^{-1}, & [E_M(\ell)] &= 1 \text{ erg}. \end{aligned} \quad (27)$$

We have set the average magnetic field strength to approximately  $10^{12}$  G and fixed the Hall prefactor at  $1/en_e\mu_0 = 1 \text{ km}^2/\text{Myr } 10^{12} \text{ G}$ . Instead of varying these parameters, we adjusted the magnetic resistivity  $\eta$  (as shown in Table 3) to achieve a Lundquist number  $\text{Lu}$  of order 100, consistent with the magnetic field strengths typical of magnetars. Additionally, the grid consists of  $64 \times 47^2 \times 6$  mesh points, with  $n_r = 64$  radial mesh points,  $n_\xi = n_\eta = 47$  angular mesh points, and 6 patches forming the cubed-sphere structure.

In the following section, we will use  $t$  (in Myr) to represent time in MATINS simulations and the dimensionless  $\tilde{t} = \eta t/R^2$  for time in the PENCIL CODE simulations. To compare time between the two codes, it is essential to use a dimensionless quantity. Specifically, we compare the value of  $\eta t/R^2$ .

## 4. Simulations

Constructing the NS background model entails solving the Tolman-Oppenheimer-Volkoff equations (Oppenheimer & Volkoff 1939), considering a nuclear EoS at zero-temperature<sup>5</sup>. This approach involves describing both the liquid core and the solid crust of the star. Through these calculations, we can determine the thickness of the NS crust, estimated to be approximately 1 km in relation to its overall radius of about 10 km. This estimation reveals the extreme aspect ratio of the crust, approximately 1:30, with  $\mathcal{A} = (R - r_0)/\pi R$ . In our simulations conducted in Cartesian, spherical (PENCIL CODE), and cubed-sphere (MATINS) coordinates, we account for the actual aspect ratio of the NS crust.

Below, we delve into the various runs relevant to our study. We focus on simulations favoring the inverse cascade in the crust of a NS. The simulations conducted with the PENCIL CODE are detailed in Table 2, while those performed using MATINS are outlined in Table 3.

### 4.1. Reference Run

In this section, we describe the reference run in our study, run R1, performed using the PENCIL CODE in Cartesian coordinates (see Table 2). This run is constructed based on our experience and represents the optimal configuration to validate the inverse cascade in a NS crust. Run R1 is characterized by an average value of  $\text{Lu}$  on the order of a few hundred. In our Cartesian domain, the crustal shell extends from  $x = 0.9\dots 1$ ,  $y = 0\dots 1$ , and  $z = 0\dots 1$ , corresponding to spherical coordinates in the range  $r/R = 0.9\dots 1$ ,  $\theta/\pi = 0\dots 1$ , and  $\phi/\pi = 0\dots 1$ .

The initially helical magnetic field for run R1 is formulated as detailed in Section 4. Given the extreme aspect ratio ( $\mathcal{A} \approx$

<sup>5</sup> NSs consist of degenerate matter, typically characterized by temperatures lower than the Fermi temperature for their entire existence. In this specific temperature range, quantum effects, as dictated by Fermi statistics, overwhelmingly dominate over thermal effects. Therefore, the EoS for NSs can be effectively approximated as that of zero temperature, allowing us to largely ignore thermal contributions for most of their lifespan.

1:30) of the NS crust, attributed to its small thickness, our experience has shown that a sufficiently small-scale magnetic field structure is necessary to facilitate inverse cascading. As a result, the magnetic spectrum should predominantly feature small-scale structures with  $\ell_0 = k_0 R \approx 200$ . This corresponds to a wavelength  $2\pi/k_0 = 0.03 R$ , which is about one-hundredth of the latitudinal extent but only about one third of the crust's depth.

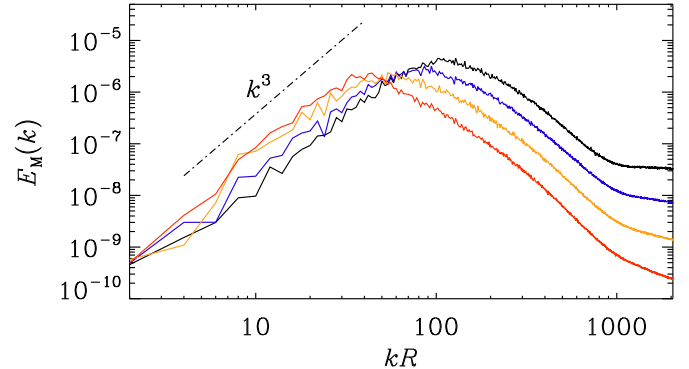


**Fig. 1.** Spectral energy of the Cartesian reference run R1. The magnetic spectra are displayed at  $\tilde{t} = 2 \times 10^{-6}$  (black),  $\tilde{t} = 6 \times 10^{-6}$  (blue),  $\tilde{t} = 2 \times 10^{-5}$  (yellow), and  $\tilde{t} = 6 \times 10^{-5}$  (red).

In Figure 1, we present magnetic energy spectra of run R1 at four distinct dimensionless times:  $\tilde{t} = 2 \times 10^{-6}$  (black),  $6 \times 10^{-6}$  (blue),  $2 \times 10^{-5}$  (yellow), and  $6 \times 10^{-5}$  (red). The magnetic field exhibits inverse cascading with a temporal decay scaling as  $k^{3/2}$  (not shown). At later times,  $\tilde{t} > 2 \times 10^{-5}$ , the spectrum of the magnetic field ceases to exhibit temporal decay, indicating that the magnetic energy is no longer dissipating. We attributed this behavior to the lower magnetic diffusion value  $\eta$  (Equation (26)), which acts in favor of enhancing the Hall-dominant evolution. For comparison, we must remember that after  $\tilde{t}_2 = 2 \times 10^{-5}$ , the value of  $\eta$  is assumed to decrease like  $\tilde{t}^{-0.4}$ , which is rather slow. As a result, at  $\tilde{t}_3 = 6 \times 10^{-5}$ ,  $\eta(\tilde{t}_3) = 1.8 \times 10^{-4}$  is only 8% below the original value and  $\text{Lu}(\tilde{t}_3) = 80$ .

Toward the end of the simulation, we notice that the inverse cascade stalls when  $\ell_0 \approx 30$ , with almost no transfer of energy toward the dipolar component. In the following sections, we will examine the impact of the coordinate system, peak wavenumber position, aspect ratio, and boundary conditions to understand what is limiting the inverse cascade from transferring energy to larger-scale structures.

### 4.2. Different coordinate systems

To study the impact of the coordinate systems on the inverse cascade, we replicated run R1 in spherical coordinates using the PENCIL CODE in run R2 (see Table 2) and in cubed-sphere coordinates using MATINS in run R5 (see Table 3). These two runs have an average value of  $\text{Lu}$  similar to that of run R1, both being on the order of a few hundred. The crustal shell is in the range  $r/R = 0.9\dots 1$  for both runs. In run R2, we choose  $\theta/\pi = 0.1\dots 0.9$  to avoid the axis singularity problem in 3D spherical coordinates, while  $\phi/\pi = 0\dots 1$ . By contrast, run R5 covers the full crustal shell and has  $\theta/\pi = 0\dots 1$ , and  $\phi/\pi = 0\dots 2$ .

The meridional slices of the  $B'(r, \theta)$  component of the magnetic field for run R2 are illustrated in Figure 2 at three different times:  $\tilde{t} = 6 \times 10^{-7}$ ,  $2 \times 10^{-6}$ , and  $6 \times 10^{-6}$  (from left to right). Initially, the magnetic spectrum predominantly features small-scale structures on the order of  $k_0 R \approx 200$  (at  $\tilde{t} = 6 \times 10^{-7}$ ). As

**Table 2.** Summary of the PENCIL CODE simulations. Cartesian simulations are indicated by ‘Cart’, while spherical simulations are denoted by ‘Sph’. Simulations with perfect conductor boundary conditions on the inner surface and vertical field boundary conditions on the outer surface in the radial directions are labeled as ‘PC-VF’. By contrast, simulations with periodic boundary conditions in the radial directions are labeled as ‘P’. The time is set to  $\tilde{t}_1 = \eta_0 t_1 / R^2 = 2 \times 10^{-6}$  and  $\tilde{t}_2 = \eta_0 t_2 / R^2 = 2 \times 10^{-5}$ . Note that  $\ell_0 = k_0 R$  for the Cartesian runs.

Run	geom/B.C.	$r/R$	$\theta/\pi$	$\phi/\pi$	$\ell_0(\tilde{t}_0)$	$\ell_0(\tilde{t}_2)$	Lu( $\tilde{t}_1$ )	Lu( $\tilde{t}_2$ )	$k_0 \xi(\tilde{t}_0)$	$\chi(\tilde{t}_0)$	Mesh points
R1	Cart/PC-VF	0.9...1	0...1	0...1	200	50	260	132	0.50	1.19	$64 \times 2048^2$
R2	Sph/PC-VF	0.9...1	0.1...0.9	0...1	200	60	251	124	0.60	1.12	$64 \times 2048^2$
R3	Cart/PC-VF	0.8...1	0...1	0...1	200	30	361	202	0.61	1.16	$128 \times 2048^2$
R4	Cart/PC-VF	0.8...1	0...0.5	0...0.5	200	10	487	272	0.61	1.15	$128 \times 1024^2$
R5	Cart/PC-VF	0.8...1	0...0.5	0...0.5	50	10	724	464	0.46	0.87	$128 \times 1028^2$
R6	Cart/P	0.9...1	0...1	0...1	200	60	283	168	0.61	1.19	$64 \times 2048^2$

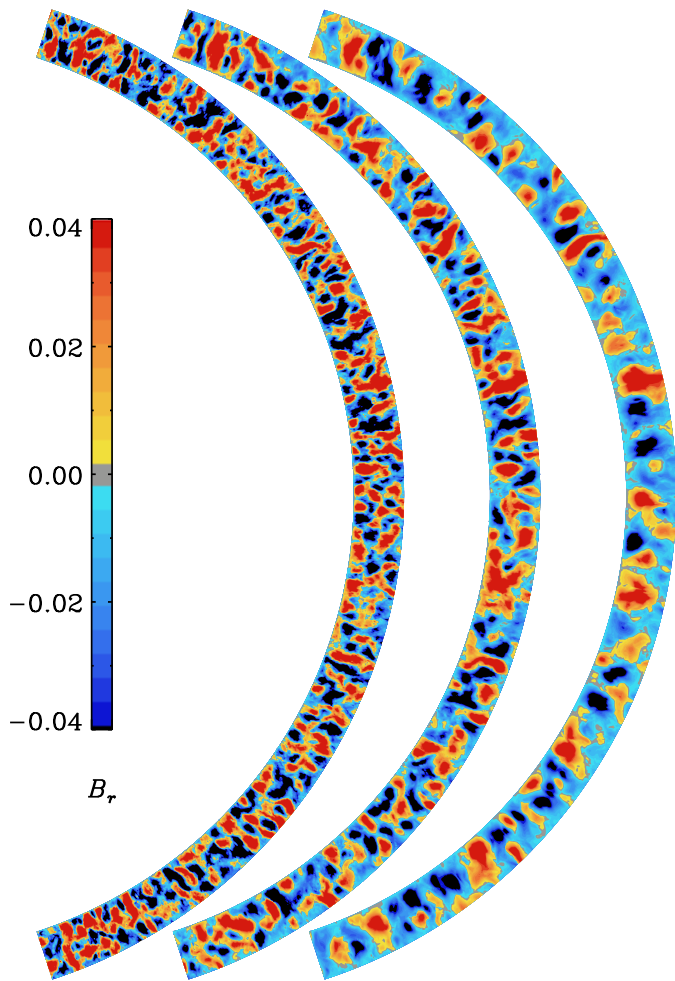


**Fig. 2.** Meridional slices of  $B'(r, \theta)$  for run R2, with  $\ell_0(\tilde{t}_0) = 200$  at  $\tilde{t} = 6 \times 10^{-7}$ ,  $2 \times 10^{-6}$ , and  $6 \times 10^{-6}$  (from left to right).

the evolution processes, the emergence of large-scale structures from small-scale ones becomes increasingly apparent, ultimately resulting in magnetic field structures comparable in size to the NS crust. This growth in scale hints at why the inverse cascade concludes, which can be attributed to the extreme aspect ratio  $\mathcal{A}$  of the NS crust. This inverse cascade in the magnetic field of run R2 is also evident in the magnetic energy spectra shown in Figure 3 at different times.

To verify if the same behavior occurs with cubed-sphere coordinates, we conducted simulations using MATINS. This test is also essential for determining if two different numerical codes yield similar results. As demonstrated previously using the PEN-

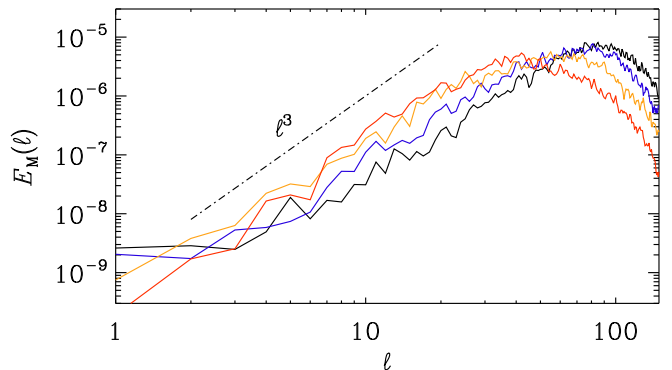


**Fig. 3.** Spectral energy of the spherical run R2. As in Figure 1, the magnetic spectra are shown at  $\tilde{t} = 2 \times 10^{-6}$  (black),  $6 \times 10^{-6}$  (blue),  $2 \times 10^{-5}$  (yellow) and  $6 \times 10^{-5}$  (red).

CIL CODE, for the inverse cascade to occur, the initial magnetic spectrum should predominantly exhibit small-scale structures with  $\ell_0 \approx 200$ . However, achieving the necessary resolution with MATINS is challenging because it is non-parallelized, unlike the PENCIL CODE.

An alternative approach involves concentrating more structures exclusively in the radial direction. This initial magnetic field configuration can be conceptualized as a squashed magnetic field structure, achieved by selecting an  $\iota$  value greater than one; see Equation (16). The  $\iota$  parameter is determined based on the results from run R1. During this run, the initial value  $\ell_0(\tilde{t}_0) \approx 200$  decreased to  $\ell_0(\tilde{t}_2) \approx 30$ . By that time, the radial scale has become  $\pi/k \approx 0.1$ , which is equal to the thickness of crust, and the inverse cascade concluded. This suggests that  $\ell$  cannot drop much below the inverse aspect ratio  $\gtrsim \mathcal{A}^{-1}$  for the inverse cascade to remain active. To cover a factor  $\mathcal{F} \approx 200/30$  for the inverse cascade in the MATINS simulations with  $\ell_{\max} = 80$ , where the affordable spherical degree would be  $\ell_0^{\text{afford}} \approx 40$ , we would need to decrease the radial scale by a squashing factor  $\iota$ . The  $\iota$  parameter can therefore be calculated using the following equation:

$$\iota \gtrsim \frac{\mathcal{F}}{\mathcal{A} \ell_0^{\text{afford}}}. \quad (28)$$

For instance, with  $\ell_0^{\text{afford}} \approx 40$  in MATINS, an  $\iota$  value of approximately 5 is necessary to accommodate  $\ell_0 \approx 200$ .

Figure 4 presents the magnetic energy spectra for the R15 simulation at four different times:  $t_0 = 0.0$  (black),  $t_1 = 0.005$  (blue),  $t_2 = 0.01$  (yellow), and  $t_3 = 0.02$  Myr (red). Similar to the Cartesian and spherical runs (R1 and R2) conducted with the PENCIL CODE, the magnetic field in run R15 exhibits an inverse

**Table 3.** Summary of MATINS simulations on a cubed-sphere grid representing a crustal shell. The time is set to  $t_0 = 0.0$ ,  $t_1 = 0.005$ ,  $t_2 = 0.01$  and  $t_3 = 0.02$  Myr, resulting in  $\eta t_1/R^2 = 6 \times 10^{-6}$  and  $\eta t_3/R^2 = 2 \times 10^{-5}$ , with  $\eta$  set to  $1.2 \times 10^{-2}$  km<sup>2</sup>/Myr. Note that in MATINS,  $\ell_0 \equiv \ell_0^{\text{afford}}$ .

Run	$r/R$	$\theta/\pi$	$\phi/\pi$	$\ell_0$	$\eta$ [km <sup>2</sup> /Myr]	$\text{Lu}(t_0)$	$\text{Lu}(t_3)$	$k_0\xi(t_0)$	$\chi(t_0)$	Mesh points
R1	0.9...1.0	0...1	0...2	40	$8 \times 10^{-3}$	60	58	0.54	0.72	$64 \times 47^2 \times 6$
R3	0.9...1.0	0...1	0...2	120	$4.5 \times 10^{-3}$	103	98	0.63	0.85	$64 \times 47^2 \times 6$
R5	0.9...1.0	0...1	0...2	200	$1.2 \times 10^{-2}$	107	90	0.64	0.92	$64 \times 47^2 \times 6$
R10	0.9...1.0	0...1	0...2	400	$1.5 \times 10^{-2}$	106	91	0.40	0.69	$64 \times 47^2 \times 6$

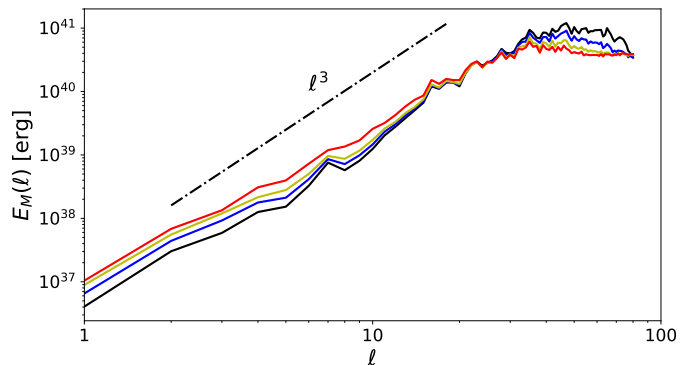


**Fig. 4.** Spectral energy of the cubed-sphere run R5 at  $t_0 = 0.0$  (black),  $t_1 = 0.005$  Myr (blue),  $t_2 = 0.01$  Myr (yellow), and  $t_3 = 0.02$  Myr (red).

cascade, featuring ascending  $\ell^3$  spectra and demonstrating temporal decay that scales as  $\ell^{3/2}$  on the cubed-sphere grid. Figure 5 shows meridional slices of the  $B^r(r, \theta)$  component of the magnetic field for run R5 at  $t = 0.0$ , 0.01 and, 0.02 Myr. The radial magnetic field structures are visibly squashed along the radial direction. Notably, the inverse cascade observed in MATINS is less pronounced than in the PENCIL CODE, as demonstrated in Figures 4 and 5. This discrepancy may be related to the  $\iota$  parameter (Equation (28)), which represents the squashing factor.

The similarity in behavior among run R1, run R2, and run R5, in Cartesian, spherical, and cubed-sphere coordinates respectively, suggests that the choice of the coordinate system is not significant, provided the correct aspect ratio is maintained. However, note that in these three models, even with different geometrical coordinates, the inverse cascade is still limited to  $\ell_0 \approx 30$ , with almost no transfer of energy toward the dipolar component.

#### 4.3. Effects of peak position

In this section, we explored the impact of different initial  $k_0R$  values on the inverse cascade using MATINS simulations. In the first case, we set  $\iota = 1$  (see Equation (28)) for run R1, resulting in  $k_0R = 40$ . In the second simulation, we increased  $\iota$  to 10 for run R10, resulting in  $k_0R = 400$ . These two simulations were conducted to verify our interpretation of the squashed initial field configuration used in MATINS and assess whether it produces the expected results.

Figure 6 displays the results for runs R1 (upper panel) and R10 (lower panel) at different evolution times. For run R1, no inverse cascade is observed, likely because the field structures are comparable to the thickness of the crust. In contrast, for run R10, the inverse cascade occurs and is more pronounced than in run R5.

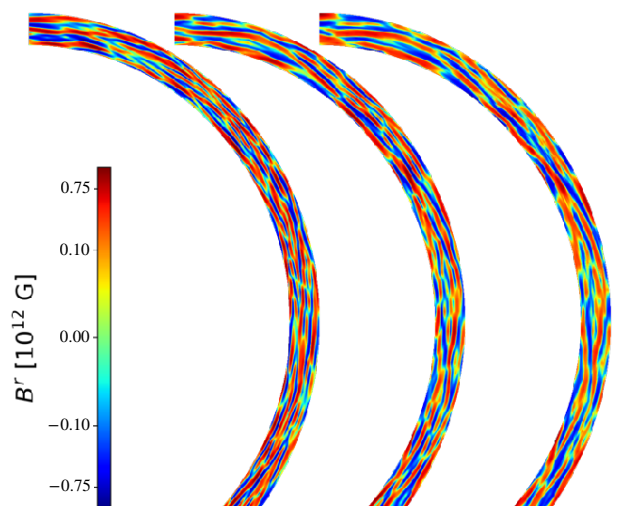


**Fig. 5.** Meridional slices of  $B^r(r, \theta)$  for run R5 at  $t = 0.0$ , 0.01 Myr and, 0.02 Myr (from left to right).

#### 4.4. Aspect ratio

To investigate the influence of the aspect ratio on the inverse cascade, we conducted a replication of the reference run R1. In this iteration, we adjusted solely the crust aspect ratio. On the one hand, in the new run R3 (see Table 2), we doubled the crustal thickness. Consequently, the crustal shell is now in the range  $r/R = 0.8...1$ , accounting for one-fifth of the entire NS cross-sectional area, as opposed to the previous one-tenth. On the other hand, in the new run R4, we also doubled the crustal thickness and, in addition, we reduced  $\theta/\pi$  and  $\phi/\pi$  from the range of 0...1 to 0...0.5. Therefore, the geometry of our domain now approaches a cubic configuration.

The magnetic energy spectra for runs R3 and R4 are depicted in the upper and lower panels of Figure 7, respectively. In this representation, magnetic spectra are plotted at  $\tilde{t} = 6 \times 10^{-7}$  (black),  $2 \times 10^{-6}$  (blue),  $6 \times 10^{-6}$  (yellow), and  $2 \times 10^{-5}$  (red). Compared to the reference run R1 (Figure 1), R3 and R4 exhibit a more pronounced inverse cascading phenomenon with several distinct behaviors.

For run R3,  $\ell_0 \approx 20$ , while for run R4,  $\ell_0 \approx 10$  at  $\tilde{t} = 2 \times 10^{-5}$ . In contrast, for run R1,  $\ell_0 \approx 50$  at the same time. Additionally, at  $\ell_0 \sim 1$ , the spectral magnetic energy tends to maintain a constant value for run R1 ( $E_M(k) \approx 6 \times 10^{-10}$ ), while runs R3 and R4 tend to accumulate energy in the dipolar component, with  $E_M(k) \approx 10^{-8}$  for run R3 and  $E_M(k) \approx 10^{-6}$  for run R4.



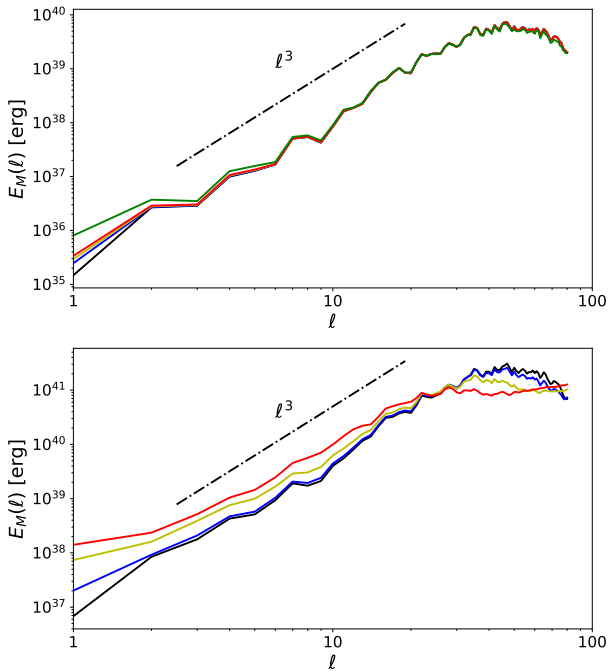


**Fig. 6.** Spectral magnetic energy for run R1 (upper panel) and run R10 (lower panel). As in Figure 4, the magnetic spectra are shown at  $t = 0.0$  (black), 0.005 (blue), 0.01 (yellow), 0.02 (red), and 0.04 Myr (green).

Furthermore, run R4 demonstrates a faster inverse cascade and dissipates less energy compared to run R3 and the reference run R1. The magnetic energy spectrum in run R4 shows a minor temporal decay, with the spectral peak  $\ell_0$  steadily maintained throughout its evolution. However, the latter behavior can be attributable to the elevated Lundquist numbers, as indicated in Table 2.

These differences with respect to the reference run R1 are attributed to the aspect ratio, especially in run R4, since its geometry approximates cubic symmetry, whereas run R3 involves doubling the crustal thickness. Alterations in crustal geometry and dimensions significantly impact the inverse cascade and the formation of the large-scale magnetic field. The realistic extreme aspect ratio of the NS crust has limited the inverse cascade and the transfer of energy toward the dipolar component.

At this stage, it is intriguing to explore whether a less extreme aspect ratio, as used in run R4, can reveal the presence or absence of an inverse cascade for a smaller  $\ell_0$ . To investigate this, we replicated run R4, adjusting  $k\ell_0$  from approximately 200 to 50 for run R5, as detailed in Table 2. The magnetic energy spectra for run R5 exhibit behavior similar to that of run R4, confirming the presence of an inverse cascade even with an initial peak wavenumber of  $\ell_0 \approx 50$ . Notably, at  $\tilde{t}_2 = 2 \times 10^{-5}$ , the peak wavenumber for both runs R4 and R5 reaches  $\ell_0 \approx 10$ , as shown in Table 2. As previously mentioned, this outcome is influenced by the crustal geometry used in both runs, which closely resembles a cubic configuration. It is important to note that starting with  $\ell_0 \approx 50$  in a model replicating the reference run R1 does not result in an inverse cascade.

#### 4.5. Periodic boundary conditions

In this section, we examine the impact of magnetic boundary conditions on our simulations. We replicated reference run R1

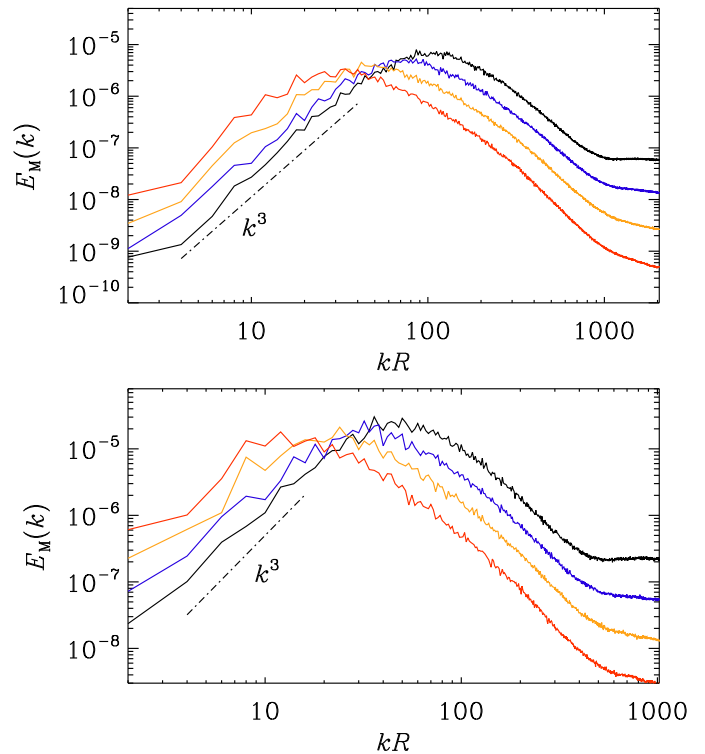


**Fig. 7.** Spectral energy of run R3 (upper panel) and run R4 (lower panel) in Cartesian coordinates, each characterized by different aspect ratios compared to the reference run R1. Data is shown at  $\tilde{t} = 6 \times 10^{-7}$  (black),  $2 \times 10^{-6}$  (blue),  $6 \times 10^{-6}$  (yellow) and  $2 \times 10^{-5}$  (red).

and modified the magnetic boundary conditions by replacing the perfect conductor and vertical field boundary conditions on the inner and outer radial boundaries, respectively, with periodic boundary conditions. This run is labeled R6, as indicated in Table 2.

The magnetic spectrum of run R6 is illustrated in Figure 8 at four distinct times. The magnetic field undergoes pronounced inverse cascading. However, unlike the reference run R1, run R6 exhibits energy transfer to low spherical degree ( $\ell_0 \sim 1$ ), with  $E_M(k) \approx 2 \times 10^{-9}$  compared to  $E_M(k) \approx 6 \times 10^{-10}$  in run R1 at  $\tilde{t} = 2 \times 10^{-5}$ . However, this energy transfer is less efficient than in runs R3 and R4. On the other hand, the inverse cascade remains limited to  $\ell_0 \approx 50$ , the same as in run R1 at  $\tilde{t} = 2 \times 10^{-5}$ . Consequently, adopting periodic boundary conditions does not explain the formation of the large-scale magnetic field in magnetars.

In contrast to the reference run R1, where the magnetic field undergoes temporal decay, run R6 exhibits a stable magnetic field with the spectral peak consistently maintained throughout its evolution. The energy spectrum of run R6 aligns with the characteristics of fully helical MHD spectra (see Figure 5 of Brandenburg (2020)). A fully helical or force-free field, characterized by a vanishing Lorentz force ( $\mathbf{J} \times \mathbf{B} = 0$ ), remains stationary due to the equilibrium implied by the force-free condition. This observation suggests that the typical boundary conditions in the NS crust result in a partially helical field, leading to a spectrum that decays as  $k^{3/2}$  (Figure 1). According to the study by Brandenburg (2017), it was found that non-periodic boundary conditions yield a field that is 78% helical. For more detail, see  $\chi$  and  $\xi$  values in Tables 2 and 3.

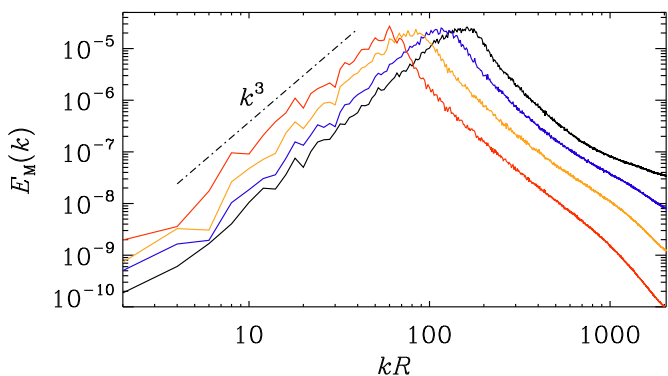


**Fig. 8.** Spectral energy of run R6 in Cartesian geometry, characterized using periodic boundary conditions compared to reference run R1. Data is shown at  $\tilde{t} = 6 \times 10^{-7}$  (black),  $2 \times 10^{-6}$  (blue),  $6 \times 10^{-6}$  (yellow), and  $2 \times 10^{-5}$  (red).

## 5. Discussion

Investigating the inverse cascade within NS crust poses a formidable challenge, with limited prior exploration in the existing literature, except for the study conducted by Brandenburg (2020). Despite this, the absence of high resolution simulations to resolve small-scale structures while accounting for the correct aspect ratio, spherical geometry, and appropriate boundary conditions, along with the consideration of time-dependent magnetic resistivity crucial due to the cooling process of NSs, was not addressed previously.

To fill this gap, our research undertook a comprehensive examination to assess the efficacy of the inverse cascade in the NS crust. Our focus extended to understanding its potential role in elucidating the origin of the large-scale dipolar field observed in magnetars — an intriguing question with substantial implications. A crucial requirement for a strong inverse cascade to occur is the presence of an initial helical magnetic field (Brandenburg 2020). Nonhelical magnetic fields can also lead to an inverse cascade from the Hall effect (Brandenburg 2023), but it is weaker. To produce an initially helical magnetic field, we developed a formalism for both Cartesian and spherical coordinates, allowing for systematic study using the PENCIL CODE and MATINS.

The slenderness of the NS crust adds complexity, necessitating initial peak wavenumbers from small-scale structures on the order of  $k_0R \approx 200$ . Resolving these scales requires high-resolution simulations, which is challenging. To overcome this, MATINS introduces additional wavenumbers in the radial direction, whereas the PENCIL CODE does not encounter this issue. However, MATINS lacks parallelization, making it less computationally powerful than the PENCIL CODE.

In our reference run, R1, we constructed a model in Cartesian coordinates with an initial helical field dominated by small-scale structures,  $k_0R \approx 200$ , while maintaining the correct aspect ratio of the NS crust (see Section 4.1). This setup was ideal for observing the inverse cascade, as the peak wavenumber shifted towards larger-scale structures within the star’s interior. However, the spectra revealed limitations, including the dissipation of the peak wavenumber, restriction of the cascade to  $k_0R \approx 30$ , and negligible energy transfer to the largest-scale structure ( $kR \approx 1$ ). To understand these phenomena, we explored the influence of geometrical coordinates, peak position, aspect ratio, and boundary conditions.

To investigate the effects of geometry, we examined different coordinate systems in Section 4.2. We used spherical coordinates in the PENCIL CODE (run R2), which requires axis adjustments to avoid singularities, and cubed-sphere coordinates in MATINS (run R4.5), which naturally circumvent this issue. Despite these variations, the outcomes remained consistent, indicating that the choice between Cartesian and spherical domains has no discernible impact when initial conditions are nearly identical. This finding supports previous research by Mitra et al. (2009). Additionally, in Section 4.3, we tested the effect of the peak position, confirming that small-scale initial spherical degrees were necessary for the inverse cascade to occur.

Expanding our analysis, we assessed the role of aspect ratio by exploring various configurations of the crustal domain (Section 4.4). In the first case (Run R3), we doubled the crustal thickness. In the second case (Run R4), we not only doubled the crustal thickness but also halved the domain in the two angular directions,  $\theta/\pi$  and  $\phi/\pi$ , resulting in a nearly cubic configuration. Compared to reference run R1, two main differences were observed: first, the peak wavenumber  $k_0R$  continued shifting toward larger-scale structures and was no longer limited to 30; second, there was a pronounced transfer of energy toward the largest-scale structure  $kR = 1$ . However, the dissipation of the peak wavenumber still occurred. These findings suggest that the thin layer of the NS crust opposes the inverse cascade, limiting the formation of a large-scale magnetic field.

Building on these findings, we then investigated how different boundary conditions affect the spectral characteristics of the inverse cascade in Section 4.5. Our results indicated that using periodic boundary conditions (run R6), rather than perfect conductor boundary conditions at the crust-core boundary or potential and vertical field boundary conditions at the surface, resulted in no dissipation of the peak wavenumber and enhanced energy transfer toward the dipolar component ( $kR = 1$ ). Periodic boundary conditions produce a fully helical magnetic field (see Brandenburg 2020), unlike other boundary conditions, which result in a partially helical field (Brandenburg 2017). A fully helical field is also a force-free field ( $\mathbf{J} \times \mathbf{B} = 0$ ), which explains the absence of dissipation in this scenario.

While periodic boundary conditions offer insights, they are not a realistic choice for studying the NS scenario. Similarly, using perfect conductor boundary conditions, which expel the field from the NS core, and vertical field or potential boundary conditions, which prevent current flow outside the star, do not fully capture the realistic conditions of magnetic field evolution in a NS crust. Carefully addressing boundary conditions is crucial for gaining a better understanding of the inverse cascade in NS crusts. Although this level of detail is beyond the scope of this paper and not feasible with the currently available numerical tools, it is important to consider for future studies.

In this study, we disregarded the temperature-dependent microphysics and the stratification within the interior of a NS crust, anticipating that these factors would not significantly impact our findings regarding the inverse cascade. The temperature-dependent microphysics is expected to reduce the magnetic diffusion parameter as the NS cools over time, leading to a higher Lundquist number (see Section 5.4 of Dehman et al. 2023b). We initiated our study with an initial Lundquist number on the order of a few hundred, simulating a magnetar-like scenario. Consequently, our Hall-dominant simulations are analogous to the evolution of magnetic fields in middle-aged magnetars.

Stratification could potentially induce variations in the magnetic diffusion and Hall prefactor, particularly in the radial direction, which might slightly alter our results. Nevertheless, the

critical factor remains the Lundquist number. To ensure a Hall-dominant simulation and the occurrence of an inverse cascade, the Lundquist number must be significantly greater than one ( $LU \gg 1$ ). Since the aspect ratio limits the inverse cascade to field structures on the order of the crustal size,  $k_0 R \approx 30$ , we expect that considering a density (or radius) dependent Lundquist number will not change this conclusion. For more on the influence of stratification on the inverse cascade, refer to Brandenburg (2020).

In light of these insights, it is essential to consider a realistic crustal thickness with the correct aspect ratio when studying the inverse cascade in a NS's crust. Although the inverse cascade cannot account for the formation of the large-scale dipolar field in magnetars, it does occur within the crust's interior on smaller scales. These findings have significant implications for NS magnetic field evolution. The field configuration identified in our study features a weak large-scale dipolar field at the star's surface with dominant small-scale structures in the interior of the crust. Additionally, the inverse cascade may contribute to the evolution of the magnetic field by transferring energy from smaller-scale to larger-scale structures, thus reducing the dissipation of small scales.

This process can potentially affect the magnetic field's configuration and stability, influencing the dynamics of the crustal lattice and potentially impacting the NS's asteroseismology (Steiner & Watts 2009; Sotani et al. 2012; Neill et al. 2023), crustal failures (Perna & Pons 2011; Pons & Perna 2011; Dehman et al. 2020) and plastic flow within the star's interior (Lander et al. 2015; Lander & Gourgouliatos 2019; Gourgouliatos & Lander 2021). The findings of our study, which began with an initial causal spectrum, align with the work of Dehman et al. (2023a), where the authors used an initial field configuration derived from core-collapse dynamo simulations to perform the long-term magneto-thermal evolution within a NS crust. These properties naturally explain key characteristics of low-field magnetars, CCOs, and high-field pulsars, which are characterized by weak dipolar magnetic fields ( $\approx 10^{12}$  G), strong small-scale fields, and enhanced magnetic activity, thereby helping to explain X-ray observational data. In summary, while the inverse cascade may not directly explain the dipolar magnetic field observed in magnetars, it plays a crucial role in other processes that influence the star's physical and observational characteristics, offering valuable insights into the complex dynamics within NSs and their astrophysical behavior.

*Acknowledgements.* We acknowledge the inspiring discussions with participants in the programs “Turbulence in Astrophysical Environments” at the Kavli Institute for Theoretical Physics, Santa Barbara (NSF PHY-2309135), and the Munich Institute for Astro-, Particle and BioPhysics (MIAPbP), which is funded by the Deutsche Forschungsgemeinschaft (DFG, German Research Foundation) under Germany's Excellence Strategy – EXC-2094 – 390783311, as well as with Jose A. Pons. We also acknowledge the visiting PhD fellow program at Nordita, which partially funded this research. This research was supported in part by the Swedish Research Council (Vetenskapsrådet) under Grant No. 2019-04234, the National Science Foundation under Grant No. AST-2307698 and the NASA ATP Award 80NSSC22K0825. We also acknowledge funding from the Conselleria d'Educació, Cultura, Universitat i Ocupació de the Generalitat Valenciana through grants CIPROM/2022/13 and ASFAE/2022/026 (with funding from NextGenerationEU PRTR-C17.11), as well as the AEI grant PID2021-127495NB-I00 funded by MCIN/AEI/10.13039/501100011033. We acknowledge the allocation of computing resources provided by the Swedish National Allocations Committee at the Center for Parallel Computers at the Royal Institute of Technology in Stockholm. *Software and Data Availability.*

The source code used for the simulations of this study, the PENCIL CODE (Pencil Code Collaboration et al. 2021), is freely available on <https://github.com/pencil-code/>. The simulation setups and corresponding input and reduced out data are freely available on <http://nor1x65.nordita.org/~brandenb/projects/Reality-InvCasc-NS>.

## References

- Akgün, T., Cerdá-Durán, P., Miralles, J. A., & Pons, J. A. 2018, *MNRAS*, 481, 5331
- Ascenzi, S., Viganò, D., Dehman, C., et al. 2024, *MNRAS*, 533, 201
- Brandenburg, A. 2017, *A&A*, 598, A117
- Brandenburg, A. 2020, *ApJ*, 901, 18
- Brandenburg, A. 2023, *JPhPh*, 89, 175890101
- Brandenburg, A. & Boldyrev, S. 2020, *ApJ*, 892, 80
- Brandenburg, A. & Kahniashvili, T. 2017, *Phys. Rev. Lett.*, 118, 055102
- Brandenburg, A., Kahniashvili, T., & Tevzadze, A. G. 2015, *PhRvL*, 114, 075001
- Brandenburg, A., Kamada, K., Mukaida, K., Schmitz, K., & Schober, J. 2023a, *Phys. Rev. D*, 108, 063529
- Brandenburg, A., Kamada, K., & Schober, J. 2023b, *PhRvR*, 5, L022028
- Brandenburg, A. & Subramanian, K. 2005, *Phys. Rep.*, 417, 1
- Chandrasekhar, S. 1981, *Hydrodynamic and Hydromagnetic Stability*, Dover Books on Physics Series (Dover Publications)
- Dehman, C. & Pons, J. A. 2024, arXiv e-prints, arXiv:2408.05281
- Dehman, C., Viganò, D., Ascenzi, S., Pons, J. A., & Rea, N. 2023a, *MNRAS*, 523, 5198
- Dehman, C., Viganò, D., Pons, J. A., & Rea, N. 2023b, *MNRAS*, 518, 1222
- Dehman, C., Viganò, D., Rea, N., et al. 2020, *ApJ*, 902, L32
- Durrer, R. & Caprini, C. 2003, *JCAP*, 2003, 010
- Esposito, P., Rea, N., & Israel, G. L. 2021, in *Astrophysics and Space Science Library*, Vol. 461, *Timing Neutron Stars: Pulsations, Oscillations and Explosions*, ed. T. M. Belloni, M. Méndez, & C. Zhang, 97–142
- Frisch, U., Pouquet, A., Léorat, J., & Mazure, A. 1975, *JFM*, 68, 769
- Geppert, U. & Wiebicke, H.-J. 1991, *A&AS*, 87, 217
- Goldreich, P. & Reisenegger, A. 1992, *ApJ*, 395, 250
- Gourgouliatos, K. N., Hollerbach, R., & Igoshev, A. P. 2020, *MNRAS*, 495, 1692
- Gourgouliatos, K. N. & Lander, S. K. 2021, *MNRAS*, 506, 3578
- Igoshev, A. P., Popov, S. B., & Hollerbach, R. 2021, *Universe*, 7, 351
- Krause, F. & Rädler, K.-H. 1980, *Mean-Field Magnetohydrodynamics and Dynamo Theory* (Oxford: Pergamon Press)
- Lander, S. K., Andersson, N., Antonopoulou, D., & Watts, A. L. 2015, *MNRAS*, 449, 2047
- Lander, S. K. & Gourgouliatos, K. N. 2019, *MNRAS*, 486, 4130
- Masada, Y., Kotake, K., Takiwaki, T., & Yamamoto, N. 2018, *Phys. Rev. D*, 98, 083018
- Mitra, D., Tavakol, R., Brandenburg, A., & Moss, D. 2009, *ApJ*, 697, 923
- Moffatt, H. K. 1978, *Magnetic Field Generation in Electrically Conducting Fluids* (Cambridge: Cambridge University Press)
- Neill, D., Preston, R., Newton, W. G., & Tsang, D. 2023, *Phys. Rev. Lett.*, 130, 112701
- Oppenheimer, J. R. & Volkoff, G. M. 1939, *PhRv*, 55, 374
- Ostriker, J. P. & Gunn, J. E. 1969, *ApJ*, 157, 1395
- Pencil Code Collaboration, Brandenburg, A., Johansen, A., et al. 2021, *JOSS*, 6, 2807
- Perna, R. & Pons, J. A. 2011, *ApJ*, 727, L51
- Pons, J. A. & Perna, R. 2011, *ApJ*, 741, 123
- Potekhin, A. Y., Pons, J. A., & Page, D. 2015, *SSRv*, 191, 239
- Reboul-Salze, A., Guilet, J., Raynaud, R., & Bugli, M. 2021, *A&A*, 645, A109
- Rogachevskii, I., Ruchayskiy, O., Boyarsky, A., et al. 2017, *ApJ*, 846, 153
- Ronchi, C., Iacono, R., & Paolucci, P. 1996, *JCoPh*, 124, 93
- Schober, J., Rogachevskii, I., Brandenburg, A., et al. 2018, *ApJ*, 858, 124
- Sigl, G. & Leite, N. 2016, *J. Cosmology Astropart. Phys.*, 2016, 025
- Sotani, H., Nakazato, K., Iida, K., & Oyamatsu, K. 2012, *Phys. Rev. Lett.*, 108, 201101
- Steiner, A. W. & Watts, A. L. 2009, *Phys. Rev. Lett.*, 103, 181101
- Thompson, C. & Duncan, R. C. 1995, *MNRAS*, 275, 255
- Turolla, R., Zane, S., & Watts, A. L. 2015, *RPPh*, 78, 116901
- Urbán, J. F., Stefanou, P., Dehman, C., & Pons, J. A. 2023, *MNRAS*, 524, 32

## Appendix A: Magnetic Formalism in 3D Spherical Coordinates

In spherical coordinates, various formalism can be used to describe the magnetic field. In this context, we present the most common notations found in the literature. For any three-dimensional solenoidal vector field  $\mathbf{B}$ , representing the magnetic field, we can always introduce the vector potential  $\mathbf{A}$  such that

$$\mathbf{B} = \nabla \times \mathbf{A}. \quad (\text{A.1})$$

The magnetic field  $\mathbf{B}$  can be expressed using the poloidal  $\Phi(\mathbf{x})$  and the toroidal  $\Psi(\mathbf{x})$  scalar functions, based on the formalism of Chandrasekhar (1981):

$$\begin{aligned} \mathbf{B}_{\text{pol}} &= \nabla \times \mathbf{A}_{\text{tor}} = \nabla \times (\nabla \times \Phi \mathbf{r}), \\ \mathbf{B}_{\text{tor}} &= \nabla \times \mathbf{A}_{\text{pol}} = \nabla \times \Psi \mathbf{r}. \end{aligned} \quad (\text{A.2})$$

Using the notation of Krause & Rädler (1980) and Geppert & Wiebicke (1991), the two scalar functions can be expanded in a series of spherical harmonics:

$$\begin{aligned} \Phi(t, r, \theta, \phi) &= \frac{1}{r} \sum_{\ell m} \Phi_{\ell m}(r, t) Y_{\ell m}(\theta, \phi), \\ \Psi(t, r, \theta, \phi) &= \frac{1}{r} \sum_{\ell m} \Psi_{\ell m}(r, t) Y_{\ell m}(\theta, \phi), \end{aligned} \quad (\text{A.3})$$

where  $\ell = 1, \dots, \ell_{\text{max}}$  is the degree and  $m = -\ell, \dots, \ell$  the order of the multipole.

The three components of the vector potential  $\mathbf{A}$  in spherical coordinates are obtained by combining the poloidal and toroidal components:

$$\begin{aligned} A^r &= \sum_{\ell m} \Psi_{\ell m}(r) Y_{\ell m}(\theta, \phi), \\ A^\theta &= \frac{1}{r \sin \theta} \sum_{\ell m} \Phi_{\ell m}(r) \frac{\partial Y_{\ell m}(\theta, \phi)}{\partial \phi}, \\ A^\phi &= -\frac{1}{r} \sum_{\ell m} \Phi_{\ell m}(r) \frac{\partial Y_{\ell m}(\theta, \phi)}{\partial \theta}. \end{aligned} \quad (\text{A.4})$$

The three components of the magnetic field  $\mathbf{B}$  in the Newtonian limit are given by:

$$\begin{aligned} B^r &= \frac{1}{r^2} \sum_{\ell m} \ell(\ell + 1) \Phi_{\ell m}(r) Y_{\ell m}(\theta, \phi), \\ B^\theta &= \frac{1}{r} \sum_{\ell m} \Phi'_{\ell m}(r) \frac{\partial Y_{\ell m}(\theta, \phi)}{\partial \theta} \\ &\quad + \frac{1}{r \sin \theta} \sum_{\ell m} \Psi_{\ell m}(r) \frac{\partial Y_{\ell m}(\theta, \phi)}{\partial \phi}, \\ B^\phi &= -\frac{1}{r} \sum_{\ell m} \Psi_{\ell m}(r) \frac{\partial Y_{\ell m}(\theta, \phi)}{\partial \theta} \\ &\quad + \frac{1}{r \sin \theta} \sum_{\ell m} \Phi'_{\ell m}(r) \frac{\partial Y_{\ell m}(\theta, \phi)}{\partial \phi}. \end{aligned} \quad (\text{A.5})$$

Here,  $\Phi'_{\ell m} = \partial \Phi_{\ell m} / \partial r$ , ignoring relativistic corrections. For the complete form, including relativistic corrections, refer to Dehman et al. (2023b). Using Equation (A.4) and Equation (A.5), one can derive the expressions for the spectral magnetic helicity Equation (7), the spectral magnetic energy Equation (8), and the spectral realisability condition Equation (9).